Improved Supertwisting Nonsingular Fast Terminal Sliding Mode Observer-Based Deadbeat Fault-Tolerant Predictive Control for IPMSM Demagnetization Fault

Dingdou Wen, Xiaorui Wei, Wenting Zhang, Sicheng Li, and Yang Zhang

***Abstract*—In this article, a deadbeat fault-tolerant predictive control (DFTPC) strategy based on the improved supertwisting nonsingular fast terminal sliding mode observer (IST-NFTSMO) is proposed. First, the IST-NFTSMO is designed by combining the improved supertwisting algorithm with the nonsingular fast terminal sliding mode (NFTSM) to observe the flux linkage and the current prediction value quickly and accurately. Based on the observed values, the DFTPC algorithm is designed to effectively compensate torque loss caused by demagnetization of permanent magnet, thus achieving fault-tolerant control. The improved supertwisting control law accelerates the convergence speed of the system and suppresses the system chattering. Second, a NFTSM controller based on improved extended supertwisting sliding mode disturbance observer (IEST-SMDO) is designed. The controller is combined with the DFPTC to further enhances the robustness and response speed of the system. Disturbances caused by demagnetization, load changes, and the action of the DFTPC algorithm in the system can be observed faster by IEST-SMDO. The observed disturbances are feedforward compensated to the speed loop controller and the immunity of the system is boosted. Finally, the experimental results show the proposed method has stronger fault tolerance and robustness than the conventional method when the IPMSM suffers from demagnetization fault.**

***Index Terms*—Demagnetization fault, fault-tolerant control, interior permanent magnet synchronous motor, nonsingular fast terminal sliding mode observer.**

I. Introduction

RECENTLY, interior permanent magnet synchronous motors (IPMSM) have been widely applied in various industrial fields, such as industrial conveying system, robot drive, wind power generation, and railway transportation due to its excellent performance and high stability [1], [2], [3], [4]. However, owing to the increase in temperature of the motor itself, or operating in complex and variable environments such as corrosion and electromagnetic interference, permanent magnet (PM) may suffer from irreversible demagnetization fault of varying degrees [5]. Among them, the effect of the motor's own temperature rise on the demagnetization of PM is more serious. At the same coercivity, the magnetic flux density amplitude of PM with high temperature is lower [6], [7], [8], [9]. After the demagnetization of the motor, the performance of its control system is seriously affected. It is possible to stop the machine to replace the PM material, but this often requires the interruption of the corresponding industrial production process, which affects the production efficiency and product quality. Moreover, in many fields such as aerospace and railway transportation, PMSM cannot be easily stopped, so it is necessary to fault-tolerant control of faulty motors to ensure their smooth operation.

The demagnetization fault detection methods of PM mainly include data-based and model-based methods. Data-based diagnosis methods include Fourier transform [10], finite element method [11], convolutional neural network [12], [13], and extreme learning machine [14], [15]. In [16], the stator current feature signal of PMSM is analyzed utilizing the fast Fourier transform to detect the demagnetization fault of the PM. This enables demagnetization fault in PM to be effectively monitored, but it is not suitable for dynamic demagnetization fault monitoring. In [17], machine learning and Fourier transform (STFT) are combined to detect demagnetization fault in IPMSM. This method is faster to detect, but the STFT is more sensitive to the noise and interference in the signals. However, data-based fault diagnosis methods rely on the computational power of the controller. Model-based methods include extended Kalman algorithm [18], model reference adaptive system (MRAS) [19], [20], and sliding mode observer (SMO) [21]. In [22], the MRAS flux observer is used for PM demagnetization detection of permanent magnet synchronous linear motors. But the design of the MRAS adaptive law is complex and susceptible to the starting values of the identification parameters, which is not conducive to practical operation. In [23], a nonsingular terminal SMO is used to detect demagnetization fault in IPMSM. However, high-frequency chattering is generated during system state tracking, which makes the system stability degraded. In [24],

Manuscript received 8 April 2024; revised 6 June 2024; accepted 4 July 2024. Date of publication 9 July 2024; date of current version 4 September 2024. This work was supported in part by the Key Research and Development Program of Hunan Province of China under Grant 2023GK2006 and in part by the Natural Science Foundation of Hunan Province of China under Grant 2023JJ50191. Recommended for publication by Associate Editor R. Kennel. *(Corresponding author: Yang Zhang.)*

The authors are with the College of Electrical and Information Engineering, Hunan University of Technology, Zhuzhou 412007, China (e-mail: wendingdou@hut.edu.cn; weixiaorui@stu.hut.edu.cn; zhangwenting@stu.hut.edu.cn; lisicheng@stu.hut.edu.cn; hut_zy@hut.edu.cn).

Color versions of one or more figures in this article are available at https://doi.org/10.1109/TPEL.2024.3425651.

Digital Object Identifier 10.1109/TPEL.2024.3425651

two integral-type terminal sliding mode observers are utilized to detect changes in the flux linkage of a five-phase IPMSM. However, it is sensitive to the initial error, and may leads to an unstable initial response of the system. In [25], multiple observers and estimation errors are utilized to calculate the flux linkage and detect demagnetization fault in PMSM. This method eliminates the impact of inductive mismatch, but its reliability rest with the accuracy of the observer output.

The above methods can effectively detect the demagnetization fault in motors, but cannot achieve fault-tolerant control when IPMSM experiences demagnetization. In [26], an improved model prediction fault-tolerant control strategy is proposed. The decoupling term related to speed is introduced into the conventional supertwisting algorithm to achieve decoupling between the speed and the system state error. Demagnetization fault can be accurately detected by improved observer and inputted into model predictive controller to update flux linkage parameters. The effect of PM demagnetization is mitigated by this method, and the control performance of the motor is improved. In [27], a fault-tolerant predictive control algorithm is proposed for online detection of the PM flux linkage. The observations of the state current are calculated based on the flux linkage observed by the SMO and is then fed back to the fault-tolerant predictive controller. The bias between the actual current value and the predicted value is eliminated, and the fault tolerance control is achieved. In [28], a model-free fault-tolerant predictive control strategy is proposed to construct a novel hyperlocal model. The unknown portion of the new hyperlocal model is estimated by the SMO. This method is fault-tolerant and robust against parameter disturbances and demagnetization fault of the motor. In [29], an integral terminal SMO-based the robust cascaded fault-tolerant predictive control method is proposed. The method takes into account the disturbances due to demagnetization fault and parameter perturbations of PMSM during modelling, which effectively avoids the rectification of the weight factors, and has strong robustness.

However, in [26], [27], [28], and [29], only the problem of the mismatch between the flux linkage and motor parameters in the speed and current loop controllers due to PM demagnetization is solved, but the problem of torque loss is not resolved. Especially when the demagnetization fault is more serious, the q-axis current has reached saturation. At this time, if only the flux linkage in the controller is updated in actual time without compensating for the missing torque, the effect of fault-tolerant control cannot be achieved.

In [30] and [31], an equivalent input disturbance method is proposed for PM demagnetization. The disturbances caused by motor demagnetization fault is effectively suppressed by this method. But if only the disturbance caused by demagnetization fault is eliminated, fault-tolerant control cannot be achieved. At this point, the electromagnetic torque still cannot keep up with the load torque. In [32], a fault-tolerant control strategy based on active flux linkage is put forward for PMSM. In this strategy, SMO is utilized to estimate the active flux linkage of the motor, and a deadbeat control method is adopted to remove the deviation of active flux linkage before and after the fault, so as to achieve fault-tolerant control. However, in this method, only the loss of the flux linkage amplitude of the PM is taken into account, and the change of magnetic deviation angle is not considered.

In this article, a deadbeat fault-tolerant predictive control (DFTPC) method based on the improved supertwisting nonsingular fast terminal sliding mode observer (IST-NFTSMO) is proposed. The method has a faster and more accurate demagnetization fault detection capability. Unlike existing methods, it can compensate for torque loss due to motor demagnetization fault. The main contributions of this study are as follows.

1) An IST-NFTSMO with faster convergence rate is designed by combining the improved supertwisting control law with nonsingular fast terminal sliding mode (NFTSM). The IST-NFTSMO can observe the flux linkage of the motor in real time more accurately and quickly, and the chattering brought by conventional NFTSMO is suppressed. The observed flux linkage is fed into the controller, allowing the effects of mismatched flux linkage parameters to be eliminated.
2) The proposed DFTPC algorithm can make the d-axis reference current of the next moment to be timely output after a demagnetization fault occurs in the motor. So that the missing torque is compensated and the sudden rise of the q-axis current is suppressed. Owing to the electromagnetic torque and q-axis current quickly recover to normal values after PM demagnetization, the fault tolerance ability of the system is further improved, and the motor can then drive larger loads.
3) To further enhance the robustness and response speed of the system, a nonsingular fast terminal sliding mode speed controller (NFTSMC) based on the improved extended supertwisting sliding mode disturbance observer (IEST-SMDO) is designed. The disturbances caused by load changes, PM demagnetization and the action of the DFTPC algorithm can be accurately observed by the IEST-SMDO in real time and compensated feed-forward, thus, the antidisturbance capability of the system is boosted.

The rest of this article is organized as follows. In Section II, the IPMSM normal and fault mathematical model is established. In Section III, the principle and implementation process of DFTPC algorithm is introduced. In Section IV, the design principle of IST-NFTSMO is explored. In Section V, the design principle of IEST-SMDO-based NFTSMC controller is discussed. In Section VI the experimental results and analysis is given. Finally, Section VII concludes this article.

II. Mathematical Model of Conventional and Demagnetized IPMSM

A. Conventional Mathematical Model of IPMSM

The conventional mathematical model of IPMSM in the dq-axis coordinate system is represented as [33]

$$\begin{cases} u_d = R_s i_d + \frac{d\psi_d}{dt} - \omega_e \psi_q \\ u_q = R_s i_q + \frac{d\psi_q}{dt} + \omega_e \psi_d \end{cases} \tag{1}$$

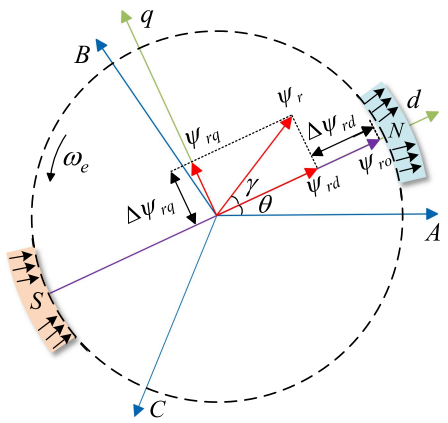

Fig. 1. Variation relationship of IPMSM flux linkage.

where *u d*, *uq*, i_d, i_q, ψ_d, and ψ_q are the *dq*-axis stator voltages, stator currents, stator flux linkages, respectively, R_s is stator resistance, ω_e is the electrical angular velocity.

The electromagnetic torque equation of IPMSM in the *dq*-axis coordinate system can be represented as

$$T_e = \frac{3}{2} n_p [\psi_{ro} + (L_d - L_q) i_d] i_q \tag{2}$$

where T_e is the electromagnetic torque, n_p is the number of pole pairs, L_d and L_q are the *dq*-axis inductances, ψ_{ro} is PM flux linkage.

The stator flux linkage is represented as follows:

$$\begin{cases} \psi_d = \psi_{ro} + L_d i_d \\ \psi_q = L_q i_q \end{cases}. \tag{3}$$

The effective flux linkage is defined as [34]

$$\psi_{ext} = \psi_{ro} + (L_d - L_q) i_d. \tag{4}$$

The mechanical equation of motion for IPMSM is represented as follows:

$$\frac{d\omega_e}{dt} = \frac{n_p}{J}(T_e - T_L - B\omega_m) \tag{5}$$

where *J* is the rotational inertia, T_L is the load torque, *B* is the viscous friction coefficient, and ω_m is the mechanical angular velocity.

B. Demagnetization Mathematical Model of IPMSM

The IPMSM due to its own temperature rise, may cause the PM demagnetization, and the amplitude of its flux will change from the initial ψ_{ro} to ψ_r. The direction of the magnetic field orientation will deviate from the direction of the flux linkage by an angle γ [35]. Therefore, two new components ψ_{rd} and ψ_{rq} will be generated on the *dq*-axis, respectively, as shown in Fig. 1. Equation (3) is rewritten as

$$\begin{cases} \psi_d = \psi_{ro} + \Delta\psi_{rd} + L_d i_d = \psi_{rd} + L_d i_d \\ \psi_q = \Delta\psi_{rq} + L_q i_q = \psi_{rq} + L_q i_q \end{cases} \tag{6}$$

where $\Delta\psi_{rd}$ and $\Delta\psi_{rq}$ are variables of the PM flux on the *dq*-axis, $\Delta\psi_{rd} = \psi_r \cos\gamma - \psi_{ro} < 0$, $\Delta\psi_{rq} = \psi_r \sin\gamma > 0$. ψ_{rd} and ψ_{rq} are two new components of ψ_r on the *dq*-axis, $\psi_{rd} = \psi_r \cos\gamma$, $\psi_{rq} = \psi_r \sin\gamma$.

Substituting (6) into (1), the demagnetization fault mathematical model of IPMSM is expressed as

$$\begin{cases} u_d = R_s i_d + L_d \frac{di_d}{dt} - \omega_e \psi_{rq} - \omega_e L_q i_q \\ u_q = R_s i_q + L_q \frac{di_q}{dt} + \omega_e (L_d i_d + \psi_{rd}). \end{cases} \tag{7}$$

Substituting (6) into (2), the electromagnetic torque equation for demagnetization fault of IPMSM is represented as follows:

$$T_e = \frac{3}{2} n_p [\psi_{rd} i_q + (L_d - L_q) i_d i_q - \psi_{rq} i_d]. \tag{8}$$

III. Design of DFTPC Strategy

Deadbeat control can theoretically realize the real values of the controlled variable are exactly the same as the given values in one or several control cycles, and can achieve the precise control of the motor torque. When IPMSM is demagnetized, it can be seen from (8) that to keep T_e unchanged will inevitably cause a sudden rise of i_q. However, at this time, i_q is close to saturation, and the missing T_e cannot be compensated by adjusting i_q, fault-tolerant control can only be achieved by adjusting i_d. Based on the above idea, make the effective flux linkage after a fault track to the prefault value within one control cycle, thus, the missing T_e is compensated by adjusting the i_d.

From (6), the flux linkage equation for the demagnetization fault of the IPMSM is represented as

$$\begin{cases} \psi_d = \psi_{rd} + L_d i_d = \psi_{ext-f} + L_q i_d \\ \psi_q = \psi_{rq} + L_q i_q \end{cases} \tag{9}$$

where $\psi_{ext\text{-}f}$ is the effective flux linkage of the PM after demagnetization $\psi_{ext-f} = \psi_{rd} + (L_d - L_q) i_d$.

Substituting (9) into (1) yields

$$\begin{cases} \dot{\psi}_d = -\frac{R_s}{L_q}\psi_d + \omega_e \psi_q + u_d + \frac{R_s}{L_q}\psi_{ext-f} \\ \dot{\psi}_q = -\frac{R_s}{L_q}\psi_q - \omega_e \psi_d + u_q + \frac{R_s}{L_q}\psi_{rq}. \end{cases} \tag{10}$$

Performing first-order Eulerian discretization on (10), the demagnetization fault equation of state for the IPMSM is

$$\psi(k+1) = \epsilon(k)\psi(k) + \Gamma(k)u(k) + \mathrm{P}(k) \tag{11}$$

where $\psi(k) = [\psi_d(k) \quad \psi_q(k)]^{\mathrm{T}}$, $u(k) = [u_d(k) \quad u_q(k)]^{\mathrm{T}}$

$$\epsilon(k) = \begin{bmatrix} 1 - T_s \frac{R_s}{L_q} & T_s \omega_e(k) \\ -T_s \omega_e(k) & 1 - T_s \frac{R_s}{L_q} \end{bmatrix}, \Gamma(k) = \begin{bmatrix} T_s & 0 \\ 0 & T_s \end{bmatrix},$$

$$\mathrm{P}(k) = \begin{bmatrix} T_s \frac{R_s}{L_q} \psi_{ext-f}(k) \\ T_s \frac{R_s}{L_q} \psi_{rq}(k) \end{bmatrix}.$$

From (11), the following expression can be acquired as:

$$\psi_d(k+1) = (1 - T_s \frac{R_s}{L_q})\psi_d(k) + T_s \omega_e(k)\psi_q(k) + T_s u_d(k) + T_s \frac{R_s}{L_q}\psi_{ext-f}(k) \tag{12}$$

where T_s is the sampling period.

Performing first-order Eulerian discretization on (9), yields

$$\begin{cases}\psi_d(k) = \psi_{ext-f}(k) + L_q i_d(k) \\ \psi_q(k) = \psi_{rq} + L_q i_q(k).\end{cases} \tag{13}$$

From (13), the flux linkage equation at time k+1 can be acquired

$$\begin{cases}\psi_d(k+1) = \psi_{ext-f}(k+1) + L_q i_d^{ref}(k+1) \\ \psi_q(k+1) = \psi_{rq} + L_q i_q(k+1)\end{cases} \tag{14}$$

where $i_d^{ref}(k+1)$ is the d-axis reference current at the next time.

Substituting (13) and (14) into (12), the effective flux linkage at time k+1 is represented as

$$\psi_{ext-f}(k+1) = \psi_{ext-f}(k) + \left(1 - T_s\frac{R_s}{L_q}\right) L_q i_d(k) + T_s\omega_e(k)\psi_{rq} + T_s\omega_e(k)L_q i_q(k) + T_s u_d(k) - L_q i_d^{ref}(k+1). \tag{15}$$

From the theory of deadbeat control, let the effective flux linkage of the fault at k+1 is equivalent to the normal effective flux linkage, then (15) is rewritten as

$$\psi_{ext}(k) = \psi_{ext-f}(k) + \left(1 - T_s\frac{R_s}{L_q}\right) L_q i_d(k) + T_s\omega_e(k)\psi_{rq} + T_s\omega_e(k)L_q i_q(k) + T_s u_d(k) - L_q i_d^{ref}(k+1). \tag{16}$$

In this article, $i_d = 0$ control is used. From (4), the effective flux linkage of IPMSM without demagnetization as

$$\psi_{ext} = \psi_{ro}. \tag{17}$$

From (8), after the motor is demagnetized, an error term $(-\psi_{rq} i_d)$ appears in the T_e. At this moment, it is not reasonable to directly make the effective flux linkage at the k+1 time equal to normal ψ_{ext}. Due to the existence of the error term $(-\psi_{rq} i_d)$, the T_e after fault tolerance will be greater than the normal T_e. This will result in $i_d^{ref}(k+1)$ being larger than the ideal value, thereby causing the stator current to approach the limit value. However, the output capacity of the inverter is limited, and the stator current cannot surpass the ultimate value. So that the fault tolerance of the system will be greatly reduced. To achieve better fault tolerance for the system, a suitable Φ is necessary to be chosen instead of $\psi_{ext}(k)$ to obtain a more accurate $i_d^{ref}(k+1)$.

According to the idea of torque deadbeat control, to obtain an appropriate Φ, the T_e after the fault is made equal to the T_e before the fault, i.e.,

$$\frac{3}{2}n_p[\Phi i_q(k+1) - \psi_{rq} i_d(k+1)] = \frac{3}{2}n_p\psi_{ro} i_q(k). \tag{18}$$

From (18), Φ is obtained as

$$\Phi = \frac{\psi_{ro} i_q(k) + \psi_{rq} i_d(k+1)}{i_q(k+1)}. \tag{19}$$

In order to quickly restore the value of i_q after the demagnetization fault to normal operating value, let

$$i_q(k+1) = i_q(k). \tag{20}$$

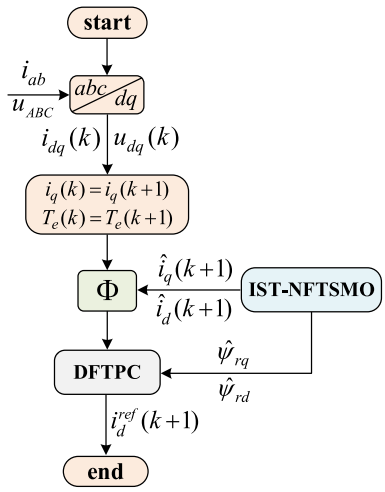

Fig. 2. Flowchart of DFTPC strategy.

Substituting (20) into (19), Φ is obtained as

$$\Phi = \psi_{ro} + \frac{\psi_{rq} i_d(k+1)}{i_q(k+1)}. \tag{21}$$

Replacing (21) for $\psi_{ext}(k)$ in (16), $i_d^{ref}(k+1)$can be represented as

$$i_d^{ref}(k+1) = \frac{1}{L_q}\left[\psi_{ext-f}(k) - \left[\psi_{ro} + \frac{\psi_{rq}\hat{i}_d(k+1)}{\hat{i}_q(k+1)}\right]\right] + \left(1 - \frac{R_s}{L_q}T_s\right) i_d(k) + \frac{T_s}{L_q}\left[\omega_e(k)L_q i_q(k) + u_d(k) + \omega_e(k)\psi_{rq}\right] \tag{22}$$

where $\hat{i}_d(k+1)$, $\hat{i}_q(k+1)$ are the observed current prediction value of the dq-axis currents at k+1, which are obtained from the IST-NFTSMO proposed in this article.

When IPMSM operates normally, $\psi_{rq} = 0$, $\psi_{ext\text{-}f}(k) = \psi_{ro}$. From (22), the system still adopts the control strategy of $i_d = 0$ during normal operation. When a demagnetization fault occurs, $\psi_{rq} \neq 0$, $\psi_{ext\text{-}f}(k) \neq \psi_{ro}$, then the $i_d^{ref}(k+1)$ calculated by (22) is needed to be adjusted to compensate for the lack of torque due to demagnetization. In addition, because the output capacity of the inverter is limited, $i_d^{ref}(k+1)$needs to meet the following constraints:

$$i_d^{ref} > -\sqrt{i_{s\max}^2 - i_q^2}. \tag{23}$$

The flowchart of DFTPC strategy is shown in Fig. 2.

IV. Design of IST-NFTSMO

The key to implement the DFTPC algorithm lies in the real-time observation of the PM flux linkage. In order to observe the PM flux linkage more quickly and accurately, in this section, the improved supertwisting control law is combined with NFTSM to form IST-NFTSMO. It has faster convergence speed and higher

observation accuracy, which maximizes the usefulness of the DFTPC algorithm.

A. Design and Stability Analysis of IST-NFTSMO

From (22), to obtain $i_d^{ref}(k+1)$, it is necessary to know ψ_{rd}, ψ_{rq}, $\hat{i}_d(k+1)$, and $\hat{i}_q(k+1)$. Therefore, an observer needs to be designed to observe these four variables.

From (7), the state equation can be obtained as follows:

$$\begin{cases} \dot{x} = Ax + Bu + Dd \\ y = Cx \end{cases} \tag{24}$$

where $x = [i_d \quad i_q]^{\mathrm{T}}$, $u = [u_d \quad u_q]^{\mathrm{T}}$, $y = [i_d \quad i_q]^{\mathrm{T}}$, $d = [\psi_{rd} \ \psi_{rq}]^{\mathrm{T}}$, *A, B, C, D* are the coefficient matrixes

$$A = \begin{bmatrix} -\frac{R_s}{L_d} & \omega_e \frac{L_q}{L_d} \\ -\omega_e \frac{L_d}{L_q} & -\frac{R_s}{L_q} \end{bmatrix}, \ B = \begin{bmatrix} \frac{1}{L_d} & 0 \\ 0 & \frac{1}{L_q} \end{bmatrix}, \ C = \begin{bmatrix} 1 & 0 \\ 0 & 1 \end{bmatrix},$$

$$D = \begin{bmatrix} 0 & \frac{\omega_e}{L_d} \\ -\frac{\omega_e}{L_q} & 0 \end{bmatrix}.$$

The IST-NFTSMO designed based on (24) is as follows:

$$\dot{\hat{x}} = A\hat{x} + Bu + v \tag{25}$$

where $\hat{x}$ is the observed value of x, $\hat{x} = [\hat{i}_d \quad \hat{i}_q]^{\mathrm{T}}$, $v = [v_d \quad v_q]^{\mathrm{T}}$ is the sliding mode term.

Subtracting (25) from (24), the current error state equation is as

$$\dot{e} = Ae + Dd - v \tag{26}$$

where $e = x - \hat{x}$ is the current observation error.

To enable the convergence speed of the current error to be boosted, the designed nonsingular fast terminal sliding surface is as follows:

$$s_n = \alpha e + \beta e^{m/r} + \lambda \dot{e} + \mu \dot{e}^{p/q} \tag{27}$$

where α, β, λ, μ are the positive numbers, m, r, p, q are the odd constants $1<m/r<2$, $1<p/q<2$, $m/r<p/q$.

The derivation of (27), the following expression is obtained:

$$\dot{s}_n = \alpha \dot{e} + \frac{m}{r}\beta e^{m/r-1}\dot{e} + \lambda \ddot{e} + \frac{p}{q}\mu \dot{e}^{p/q-1}\ddot{e}. \tag{28}$$

To accelerate the arrival of system state variables on the sliding mode surface, the improved supertwisting control law introduced is as follows [36]:

$$\begin{cases} \dot{s}_n = -k_1 |s_n|^{0.5} \mathrm{sgn}(s_n) - k_2 s_n + \sigma \\ \dot{\sigma} = -k_3 \mathrm{sgn}(s_n) - k_4 \sigma \end{cases} \tag{29}$$

where k_1, k_2, k_3, k_4 are all positive numbers to be designed, sgn(.) is the symbol function, and σ is the auxiliary variable.

In [26], the decoupling of the speed and the system state error is realized by introducing a decoupling term related to speed in the supertwisting. But the parameter sensitivity of the system is increased. The approach proposed in this article introduces a closed-loop feedback term in the conventional supertwisting. The feedback of σ allows the dynamic response of the system to be improved, thus accelerating the arrival of the system state variables to the sliding mode surface. Meanwhile, the dynamical couple relation between s_n and σ is unchanged to maintain the basic tuning performance of the conventional supertwisting algorithm unchanged.

The designed IST-NFTSMO control law is represented as

$$\begin{cases} v = v_{eq} + v_n \\ v_{eq} = Ae \\ v_n = \int_0^t \left[\frac{\alpha \dot{e} + \frac{m}{r}\beta e^{m/r-1}\dot{e}}{\frac{p}{q}\mu \dot{e}^{p/q-1} + \lambda} + k_1 |s_n|^{0.5} \mathrm{sgn}(s_n) + k_2 s_n - \sigma \right] d\tau \\ \dot{\sigma} = -k_3 \mathrm{sgn}(s_n) - k_4 \sigma \end{cases} \tag{30}$$

where v_n is the switching control law, it improves the state variable to reach the sliding mode surface quickly. And v_{eq} is the equivalent control law, it ensures the state variable continues to remain on the sliding mode surface $s_n = 0$ after reaching the sliding surface.

Theorem 1: For the error state equation of (26), by choosing the nonsingular fast terminal sliding mode surface (27) and the improved supertwisting control law (29), the IST-NFTSMO control law is designed as (30), then e converges in finite time.

Assumption 1: $|D\dot{d}|$ is bounded and $k_1 |s_n|^{0.5} - |D\dot{d}| \geq 0$, $k_2 |s_n| - |D\dot{d}| \geq 0$.

Proof: The selected Lyapunov function V_1 is as follows:

$$V_1 = \frac{1}{2} s_n^2. \tag{31}$$

Taking the derivative of (31), the following expression is obtained:

$$\begin{aligned} \dot{V}_1 = s_n \dot{s}_n &= s_n \left[\alpha \dot{e} + \frac{m}{r}\beta e^{m/r-1}\dot{e} + \left(\lambda + \frac{p}{q}\mu \dot{e}^{p/q-1} \right) \ddot{e} \right] \\ &= s_n \left[\left(\lambda + \frac{p}{q}\mu \dot{e}^{p/q-1} \right) \left(\ddot{e} + \frac{\left(\alpha + \frac{m}{r}\beta e^{m/r-1} \right) \dot{e}}{\lambda + \frac{p}{q}\mu \dot{e}^{p/q-1}} \right) \right]. \end{aligned} \tag{32}$$

Derivating of (26), the following expression is obtained:

$$\ddot{e} = A\dot{e} + D\dot{d} - \dot{v}. \tag{33}$$

Substituting (33) into (32), the following expression is as:

$$\begin{aligned} \dot{V}_1 = s_n &\left(\lambda + \frac{p}{q}\mu \dot{e}^{p/q-1} \right) \\ &\times \left[\left(A\dot{e} + D\dot{d} - \dot{v} + \frac{\left(\alpha + \frac{m}{r}\beta e^{m/r-1} \right) \dot{e}}{\lambda + \frac{p}{q}\mu \dot{e}^{p/q-1}} \right) \right]. \end{aligned} \tag{34}$$

Taking the derivative of (30), the following expression is obtained:

$$\begin{cases} \dot{v} = A\dot{e} + \frac{\alpha \dot{e} + \frac{m}{r}\beta e^{m/r-1}\dot{e}}{\frac{p}{q}\mu \dot{e}^{p/q-1} + \lambda} + k_1 |s_n|^{0.5} \mathrm{sgn}(s_n) + k_2 s_n - \sigma \\ \dot{\sigma} = -k_3 \mathrm{sgn}(s_n) - k_4 \sigma. \end{cases} \tag{35}$$

Substituting (35) into (34), the following expression is as:

$$\begin{aligned} \dot{V}_1 = &- \left(\lambda + \frac{p}{q}\mu \dot{e}^{p/q-1} \right) \Big[s_n \left(-D\dot{d} + k_1 |s_n|^{0.5} \mathrm{sgn}(s_n) \right. \\ &\left. + k_2 s_n \sigma \right) \Big] \end{aligned}$$

$$= -\left(\lambda + \frac{p}{q}\mu\dot{e}^{p/q-1}\right)\left[\left(-D\dot{d}\cdot s_n + s_n\cdot k_1|s_n|^{1.5} + k_2 s_n^2 - \sigma\cdot s_n\right)\right]$$
$$= -\left(\lambda + \frac{p}{q}\mu\dot{e}^{p/q-1}\right)\left[\left(k_2 s_n^2 - \sigma\cdot s_n + |s_n|\left(k_1|s_n|^{0.5} - D\dot{d}\right)\right)\right]. \quad (36)$$

Equation (36) can also be expressed as

$$\dot{V}_1 = -\left(\lambda + \frac{p}{q}\mu\dot{e}^{p/q-1}\right)\left[\left(k_1|s_n|^{1.5} - \sigma\cdot s_n + |s_n|\left(k_2|s_n| - D\dot{d}\right)\right)\right]. \quad (37)$$

Because $p/q>0$, $\dot{e}^{(p/q)-1} > 0$, $k_2>0$, σ is the opposite sign of s_n, it can be inferred by Assumption 1 and (36) that

$$\dot{V}_1 = -\left(\lambda + \frac{p}{q}\mu\dot{e}^{p/q-1}\right)\left[\left(k_2 s_n^2 - \sigma\cdot s_n + |s_n|\left(k_1|s_n|^{0.5} - D\dot{d}\right)\right)\right]$$
$$\le -\left(\lambda + \frac{p}{q}\mu\dot{e}^{p/q-1}\right)\left[\left(k_2 s_n^2 - \sigma\cdot s_n + |s_n|\left(k_1|s_n|^{0.5} - \left|D\dot{d}\right|\right)\right)\right]$$
$$\le -\left(\lambda + \frac{p}{q}\mu\dot{e}^{p/q-1}\right)\left(k_2 s_n^2 - \sigma\cdot s_n\right) \le 0. \quad (38)$$

Because $k_1>0$, it can be inferred by Assumption 1 and (37) that

$$\dot{V}_1 = -\left(\lambda + \frac{p}{q}\mu\dot{e}^{p/q-1}\right)\left[\left(k_1|s_n|^{1.5} - \sigma\cdot s_n + |s_n|\left(k_2|s_n| - D\dot{d}\right)\right)\right]$$
$$\le -\left(\lambda + \frac{p}{q}\mu\dot{e}^{p/q-1}\right)\left[\left(k_1|s_n|^{1.5} - \sigma\cdot s_n + |s_n|\left(k_2|s_n| - \left|D\dot{d}\right|\right)\right)\right]$$
$$\le -\left(\lambda + \frac{p}{q}\mu\dot{e}^{p/q-1}\right)\left(k_1|s_n|^{1.5} - \sigma\cdot s_n\right) \le 0. \quad (39)$$

From (39), it can be seen $\dot{V}_1 \le 0$, so the state variables will reach the sliding mode surface in limited time, and the designed observer can achieve the stabilization condition.

B. Observation of Flux Linkage and I_d (k+1)

When the system enters the sliding mode, it can be inferred that

$$\dot{e} = e = 0. \quad (40)$$

Substituting (40) into (26) gives

$$Dd = v. \quad (41)$$

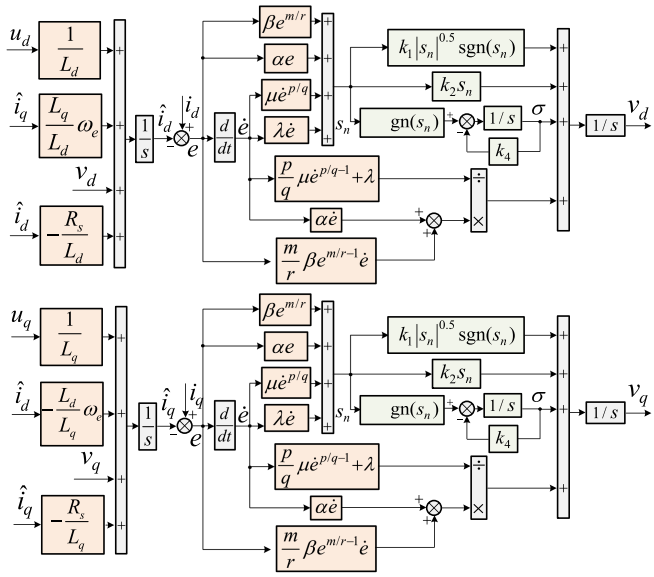

Fig. 3. Block diagram of IST-NFTSMO.

Therefore, the observed values of the dq-axis flux linkages can be represented as

$$\begin{cases}\hat{\psi}_{rd} = \frac{-v_q\cdot L_d}{\omega_e}\\ \hat{\psi}_{rq} = \frac{v_d\cdot L_q}{\omega_e}\end{cases} \quad (42)$$

where v_d, v_q are the sliding mode control laws for the dq-axis, respectively.

From (25), the observed value of the predicted current at the next time can be represented as

$$\begin{cases}\hat{i}_d(k+1) = \left(1 - \frac{R_s}{L_d}T_s\right)\hat{i}_d(k) + \frac{T_s}{L_d}\\ \left(u_d(k) + \omega_e(k)L_q\hat{i}_q(k) + L_d v_d\right)\\ \hat{i}_q(k+1) = \left(1 - \frac{R_s}{L_q}T_s\right)\hat{i}_q(k) + \frac{T_s}{L_q}\\ \left(u_q(k) + \omega_e(k)L_d\hat{i}_d(k) + L_q v_q\right)\end{cases} \quad (43)$$

where $\hat{i}_d(k)$ and $\hat{i}_q(k)$ are the observed value of dq-axis currents at the current moment.

The block diagram of IST-NFTSMO is shown in Fig. 3.

V. Design of NFTSMC Controller Based on IEST-SMDO

Considering the effects generated by load changes, PM demagnetization and the action of the DFTPC algorithm, in order to achieve high-performance control of the IPMSM in the demagnetized state and to accelerate the speed dynamic response. In this section, an IEST-SMDO-based NFTSMC speed controller is designed by taking into account the above disturbances in the establishment of the speed loop model. Where IEST-SMDO estimates the disturbances in the system generated by load changes, PM demagnetization and the action of the DFTPC algorithm in real time by measuring the inputs and outputs of the actual system, while feed-forward compensation of the NFTSMC is

performed to improve the robustness and response speed of the system.

A. Design of NFTSMC Controller

From (5) and (8), the mechanical equation of motion for the demagnetization fault is given by

$$\frac{d\omega_m}{dt} = \frac{3}{2}\frac{n_p}{J}\left[\psi_{ro}i_q + (L_d - L_q)i_d i_q + \Delta\psi_{rd}i_q - \psi_{rq}i_d\right] - \frac{1}{J}(T_L + B\omega_m). \tag{44}$$

Equation (44) is rewritten as

$$\frac{d\omega_m}{dt} = \frac{3}{2}\frac{n_p}{J}\psi_{ro}i_q - \frac{B}{J}\omega_m - \frac{1}{J}\Delta d\,(t) \tag{45}$$

where $\Delta d(t)$ is the aggregate disturbance of the control system, $\Delta d(t) = T_L$-$1.5n_p\Delta T_e$ including the load disturbance, the demagnetization fault disturbance, and the disturbance caused by the action of DFTPC algorithm. ΔT_e is the electromagnetic torque variable resulting from demagnetization fault as well as the action of i_d^{ref}, $\Delta T_e = (L_d$-$L_q)i_d i_q$+$\Delta\psi_{rd}i_q$-$\psi_{rq}i_d$.

The reference speed is defined as ω_{ref}, and the actual speed is defined as ω_m, the speed error and error change rate are as follows:

$$\begin{cases} e_m = \omega_{ref} - \omega_m \\ \dot{e}_m = \dot{\omega}_{ref} - \dot{\omega}_m \end{cases}. \tag{46}$$

To enable the convergence speed of the system state to be boosted, the nonsingular fast terminal sliding mode surface selected is as follows:

$$s_m = e_m + a\int_0^t e_m d\tau + b\int_0^t |e_m|^c\,\mathrm{sgn}(e_m)d\tau \tag{47}$$

where a>0, b>0, 0<c<1.

Derivation of (47)

$$\dot{s}_m = \dot{e}_m + ae_m + b|e_m|^c\mathrm{sgn}(e_m). \tag{48}$$

Substituting (45) into (48) gives

$$\dot{s}_m = -\frac{3}{2}\frac{n_p}{J}\psi_{ro}i_q + \frac{B\omega_m}{J} + \frac{\Delta d\,(t)}{J} + ae_m + b|e_m|^c\mathrm{sgn}(e_m). \tag{49}$$

To enhance the system convergence speed and suppresses the chattering, a new exponential approach law is introduced. On this basis, the Sigmoid(.) function is used instead of the sgn(.) function, and the system state variables are introduced in the exponential term. The sliding mode surface will change with the state of the system, and the inherent chattering of sliding mode can be diminished

$$\begin{cases} \dot{s}_m = -\varepsilon\varepsilon_1\left(1 - e^{-h|s_m|^g}\right)\left(\frac{2}{1+e^{-\eta s_m}} - 1\right) - k|x|^n s_m \\ \lim\limits_{t\to\infty}|x| = 0 \end{cases} \tag{50}$$

where ε>0, ε_1>1, η>0, h>0, g>0, k>0, n>0. s_m is the sliding mode surface defined by the system, and x is the state variable e_m of the system.

Theorem 2: For the error state equation of (46), by choosing the nonsingular fast terminal sliding mode surface (47) and the novel exponential approach law (50), the control law of NFTSMC controller is designed as (51), then e_m converges in finite time

$$u_m = \frac{1}{D}\begin{bmatrix} \frac{\Delta\hat{d}(t)}{J} + \frac{B\omega_m}{J} + ae_m + b|e_m|^c\mathrm{sgn}(e_m) \\ +\varepsilon\varepsilon_1\left(1 - e^{-h|s_m|^g}\right)\left(\frac{2}{1+e^{-\eta s_m}} - 1\right) + k|e_m|^n s_m \end{bmatrix} \tag{51}$$

where $D = \frac{3n_p\psi_{ro}}{2J}$, $u_m = i_q$, and $\Delta\hat{d}(t)$is the observed value of the aggregate disturbance in the system.

Assumption 2: $\varepsilon\varepsilon_1(1 - e^{-h|s_m|^g}) - (\|\frac{\Delta\tilde{d}(t)}{J}\| + \rho) \geq 0$, $\rho > 0$.

Proof 2: The selected Lyapunov function V_2 is as follows:

$$V_2 = \frac{1}{2}s_m^2. \tag{52}$$

Taking the derivative of (52) and substituting (48) and (49) into (52) gives

$$\begin{aligned} \dot{V}_2 &= s_m\dot{s}_m = s\left[\dot{e}_m + ae_m + b|e_m|^c\mathrm{sgn}(e_m)\right] \\ &= s_m\left[-\frac{3}{2}\frac{n_p}{J}\psi_{ro}u_m + \frac{B\omega_m}{J} + \frac{\Delta d\,(t)}{J} + ae_m + b|e_m|^c\mathrm{sgn}(e_m)\right] \\ &= s_m\left(-\frac{\Delta\hat{d}\,(t)}{J} + \frac{\Delta d\,(t)}{J} - \varepsilon\varepsilon_1\left(1 - e^{-h|s_m|^g}\right)\left(\frac{2}{1+e^{-\eta s_m}} - 1\right) - k|e_m|^n s_m\right) \\ &= s_m\left(\frac{\Delta\tilde{d}\,(t)}{J} - \varepsilon\varepsilon_1\left(1 - e^{-h|s_m|^g}\right)\left(\frac{2}{1+e^{-\eta s_m}} - 1\right) - k|e_m|^n s_m\right) \end{aligned} \tag{53}$$

where $\Delta\tilde{d}(t)$ is the aggregate disturbance error of the system and is bounded, $\Delta\tilde{d}(t) = \Delta d(t) - \Delta\hat{d}(t)$.

Since ε>0, ε_1>1, $0 \leq 1 - e^{-h|s_m|^g} < 1$, k>0, $|e_m|^n \geq 0$, according to Assumption 1 and (53), it can be concluded that

$$\begin{aligned} \dot{V}_2 &= s_m\left(\frac{\Delta\tilde{d}\,(t)}{J} - \varepsilon\varepsilon_1\left(1 - e^{-h|s_m|^g}\right)\left(\frac{2}{1+e^{-\eta s_m}} - 1\right) - k|e_m|^n s_m\right) \\ &\leq \left(\left\|\frac{\Delta\tilde{d}\,(t)}{J}\right\| - \varepsilon\varepsilon_1\left(1 - e^{-h|s_m|^g}\right)\right)\|s_m\| - k|e_m|^n\|s_m\|^2 \leq 0. \end{aligned} \tag{54}$$

From (54), it can be seen $\dot{V}_2 \leq 0$, so the state variables will arrive the sliding mode surface in limited time, and the designed controller is able to achieve stability condition.

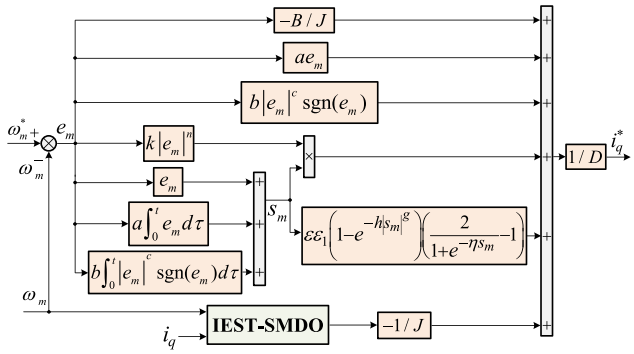

Fig. 4. Block diagram of NFTSMC based on IEST-SMDO.

The block diagram of the IEST-SMDO-based NFTSMC is shown in Fig. 4.

B. Design of IEST-SMDO

IEST-SMDO estimates the disturbances caused by loads, demagnetization fault, and the action of the DFTPC algorithm in actual time, and feedforward compensates the NFTSMC. Thus, the fault tolerance and robustness of the system is boosted.

The IEST-SMDO constructed by (45) is as follows:

$$\begin{cases} \frac{d\hat{\omega}_m}{dt} = \frac{3}{2}\frac{n_p}{J}\psi_{ro} i_q - \frac{B}{J}\hat{\omega}_m - \frac{1}{J}\Delta\hat{d}(t) + u_w \\ \frac{d[\Delta\hat{d}(t)]}{dt} = G u_w \end{cases} \tag{55}$$

where $\hat{\omega}_m$ is the observed value of ω_m, G is the sliding mode coefficient $G>0$, and u_w is the sliding mode control law.

The selected sliding surface is shown below

$$e_n = \hat{\omega}_m - \omega_m. \tag{56}$$

Taking the derivative of (56) yields

$$\begin{cases} \dot{e}_n = -\frac{B}{J}e_n + \tilde{F} + u_w \\ \dot{\tilde{F}} = G u_m - \xi(t) \end{cases} \tag{57}$$

where $\tilde{F}$ is the rate of change of F, $\tilde{F} = \frac{\Delta d(t)}{J} - \frac{\Delta\hat{d}(t)}{J}$, $\xi(t) = \frac{dF}{dt}$.

Theorem 3: By selecting the speed observation error e_n as the state variable and introducing the improved supertwisting (29), the IEST-SMDO control law is designed as (58), and e_n converges in finite time

$$\begin{cases} u_m = -k_a|e_n|^{0.5}\mathrm{sgn}(e_n) - \left(k_b - \frac{B}{J}\right)e_n + \sigma_1 \\ \dot{\sigma}_1 = -k_c\mathrm{sgn}(e_n) - k_d\sigma_1 \end{cases} \tag{58}$$

where k_a, k_b, k_c, k_d are the positive numbers to be designed, σ_1 is the auxiliary variable.

Assumption 3: $k_a|e_n|^{0.5} - |\tilde{F}| \geq 0$, $k_b|e_n| - |\tilde{F}| \geq 0$, $|\tilde{F}|$ is bounded.

Proof 3: The selected Lyapunov function V_3 is as follows:

$$V_3 = \frac{1}{2}{e_n}^2. \tag{59}$$

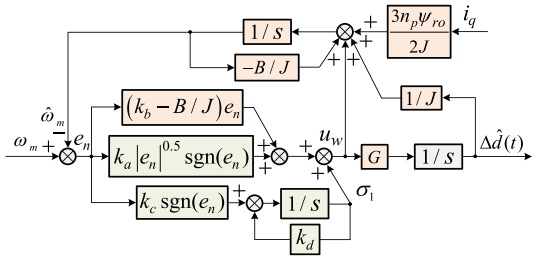

Fig. 5. Block diagram of IEST-SMDO.

Taking the derivative of (59) and substituting (57) into (59) gives

$$\begin{aligned} \dot{V}_3 &= e_n\dot{e}_n = e_n\left(-\frac{B}{J}e_n + \tilde{F} + u_w\right) \\ &= e_n\left(-\frac{B}{J}e_n + \tilde{F} - k_a|e_n|^{0.5}\mathrm{sgn}(e_n) - \left(k_b - \frac{B}{J}\right)e_n + \sigma_1\right) \\ &= -e_n\left(-\tilde{F} + k_a|e_n|^{0.5}\mathrm{sgn}(e_n) + k_b e_n - \sigma_1\right) \\ &= -\left(-\tilde{F}\cdot e_n + k_a|e_n|^{0.5}\mathrm{sgn}(e_n)\cdot e_n + k_b e_n\cdot e_n - \sigma_1\cdot e_n\right) \\ &= -\left(k_b e_n^2 - \sigma_1\cdot e_n + |e_n|\left(k_a|e_n|^{0.5} - \tilde{F}\right)\right). \end{aligned} \tag{60}$$

Equation (60) can also be expressed as

$$\dot{V}_3 = -\left(k_a|e_n|^{1.5} - \sigma_1\cdot e_n + |e_n|\left(k_b|e_n| - \tilde{F}\right)\right). \tag{61}$$

Because $k_a>0$, $k_b>0$, σ_1 is the opposite sign of e_n, according to Assumption 3 and (60), it can be concluded that

$$\begin{aligned} \dot{V}_3 &\leq -\left(k_b e_n^2 - \sigma_1\cdot e_n + |e_n|\left(k_a|e_n|^{0.5} - \left|\tilde{F}\right|\right)\right) \\ &\leq -\left(k_b e_n^2 - \sigma_1\cdot e_n\right) \leq 0. \end{aligned} \tag{62}$$

From Assumptions 3 and (61), it can be concluded that

$$\begin{aligned} \dot{V}_3 &\leq -\left(k_a|e_n|^{1.5} - \sigma_1\cdot e_n + |e_n|\left(k_b|e_n| - \left|\tilde{F}\right|\right)\right) \\ &\leq -\left(k_a|e_n|^{1.5} - \sigma_1\cdot e_n\right) \leq 0. \end{aligned} \tag{63}$$

From (63), it can be seen $\dot{V}_3 \leq 0$, so the state variables will reach the sliding mode surface in limited time, and the designed observer can achieve the stabilization condition.

The block diagram of IEST-SMDO is shown in Fig. 5.

The system block diagram of IST-NFTSMO-based DFTPC is shown in Fig. 6.

VI. Experimental Results and Analysis

Since the demagnetization fault of IPMSM is difficult to simulate in real motors, to validate whether the proposed method is effective and feasible, this article adopts RT-LAB to establish the hardware in the loop simulation experiment (hardware in the loop simulation, HILS) platform without affecting the experimental results. The schematic diagrams are shown in Figs. 7 and 8. The DSP utilizes the TMS320F2812, and the IPMSM and its demagnetization fault are constructed by RT-LAB (OP5600).

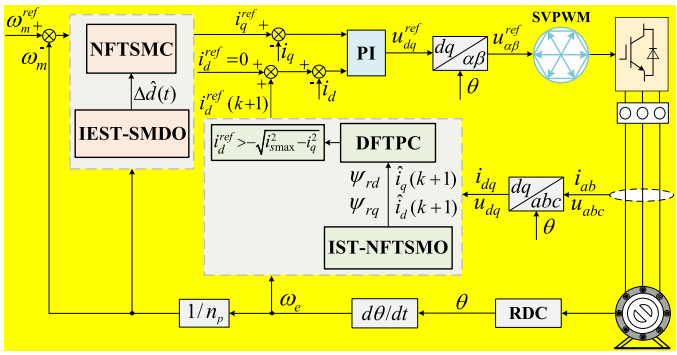

Fig. 6. System block diagram of IST-NFTSMO-based DFTPC.

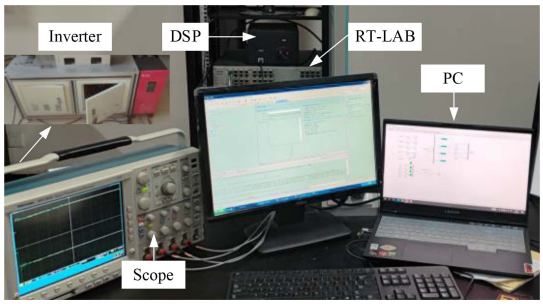

Fig. 7. RT-LAB experiment platform.

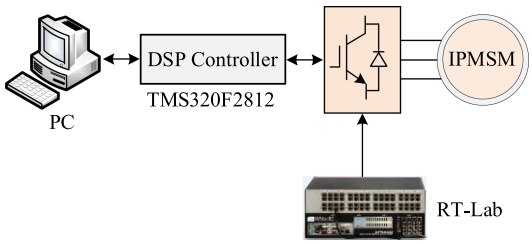

Fig. 8. RT-LAB hardware-in-the-loop system configuration.

The IPMSM's control strategy adopts $i_d = 0$. The parameters of IPMSM are given in Table I, the control parameters for all control methods are shown in Table II, and the observer parameters are shown in Table III.

First, the three methods, proportional integral (PI) control, sliding mode control (SMC) and the proposed IEST-SMDO-based NFTSMC are compared without using the proposed DFTPC algorithm. Second, the PI control, SMC and the IEST-SMDO-based NFTSMC are combined with the DFTPC algorithm to obtain the methods of DFTPC-PI, DFTPC-SMC, and DFTPC-IEST-SMDO-NFTSMC, respectively. The proposed DFTPC-IEST-SMDO-NFTSMC method is tested against both DFTPC-PI and DFTPC-SMC.

A. IPMSM Control Without DFTPC Algorithm

In order to compare the three methods (PI, SMC, and the proposed IEST-SMDO-based NFTSMC) without using the proposed DFTPC algorithm, the working conditions are set as follows.

TABLE I
PARAMETERS OF IPMSM

Parameters	Values	Unit
Number of pole pairs (n_p)	4	
Stator resistance (R_s)	0.02	Ω
q-axis inductance (L_q)	0.003572	H
d-axis inductance (L_d)	0.0015	H
PM flux linkage (ψ_{ro})	0.892	Wb
Dc voltage (U_{dc})	1500	V
Rated torque (T_N)	1008	N· m
Rotational inertia (J)	1	kg· m^2
Viscous friction coefficient (B)	0.001	N· m· s/rad

TABLE II
PARAMETERS OF THE CONTROL SYSTEM

PI	SMC	NFTSMC
$k_p = 150$	$k_1 = 20\,000$	$a = 0.02$
$k_i = 5000$	$k_2 = 1000$	$b = 0.04$
-	-	$c = 0.1$
-	-	$\varepsilon_1 = 2$
-	-	$\varepsilon = 180$
-	-	$h = 3$
-	-	$g = 3$
-	-	$\eta = 0.8$
-	-	$k = 2190$
-	-	$n = 0.1$

Remark 1: *The current loop PI parameters are first calibrated according to the type I system, then the current loop is equivalent to a link in the speed loop, and finally the speed loop PI parameters are calibrated and fine-tuned according to the type II system.*

Remark 2: *k_1, k_2 (k_1>0, k_2>0), are the exponential convergence law parameter in SMC. First select a sufficiently large value to make the system converge, and then perform fine tuning.*

Remark 3: *The selection of sliding mode surface parameters in NFTSMC directly affects the stability of the motor control system. After selecting the approximate parameters of a, b,and c (a>0, b>0, 0<c<1) to confirm system stability, fine tuning is performed, a, b,and c become larger, causing the system to overshoot during transients. a, b,and c become smaller, causing a slower speed response and a longer time to reach the given value. ε, ε1 and k (ε>0, ε1>1, k>0) are the control law parameters, and the control law is to improve the dynamic quality of the convergence motion of the sliding mode variable structure. Within the specified range of the parameters, after several simulations to select the approximate appropriate ε, ε1,and k, and then fine tuning to obtain better control effect. h, g, η, and n (h>0, g>0, η>0, n>0) are used to optimize the jitter problem of the sliding mode motion.*

The total experimental time is 1 s, the motor starts with no load and the reference speed N_r^{ref} is 300 r/min. The load torque T_L is loaded from 0 to 650 N.m (65% rated load) at 0.2 s. At 0.4 s, the IPMSM is demagnetized, and the flux linkage amplitude of PM ψ_{ro} decreases from 0.892 to 0.6 Wb (demagnetization 33%), while the magnetic deviation angle γ is changed from 0 to π/6 rad.

Figs. 9, 10, and 11 show the experimental results of PI control, SMC, and the IEST-SMDO-based NFTSMC without DFTPC algorithm under demagnetization fault, respectively. Among them, Figs. 9(a), 10(a), and 11(a) show the response curves of the dq-axis currents, Figs. 9(b), 10(b), and 11(b) show the output

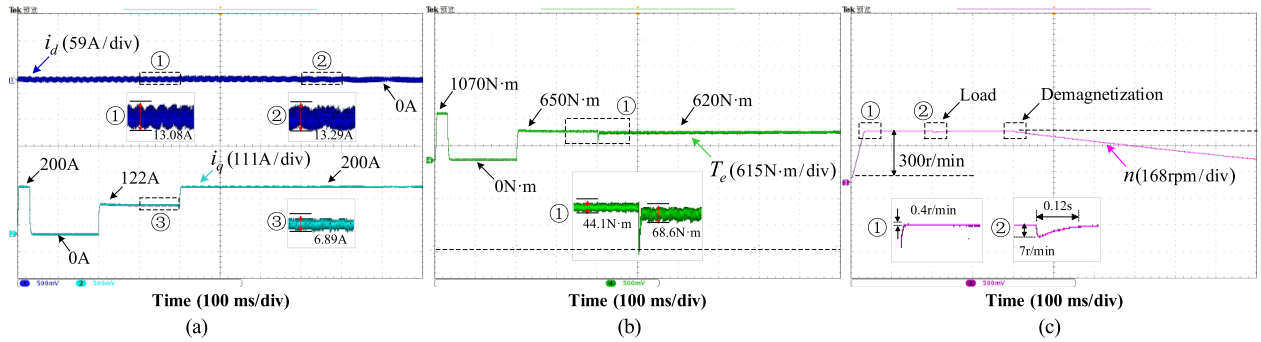

Fig. 9. Experimental results of PI control without DFTPC algorithm. (a) *dq*-axis current. (b) Electromagnetic torque. (c) Speed.

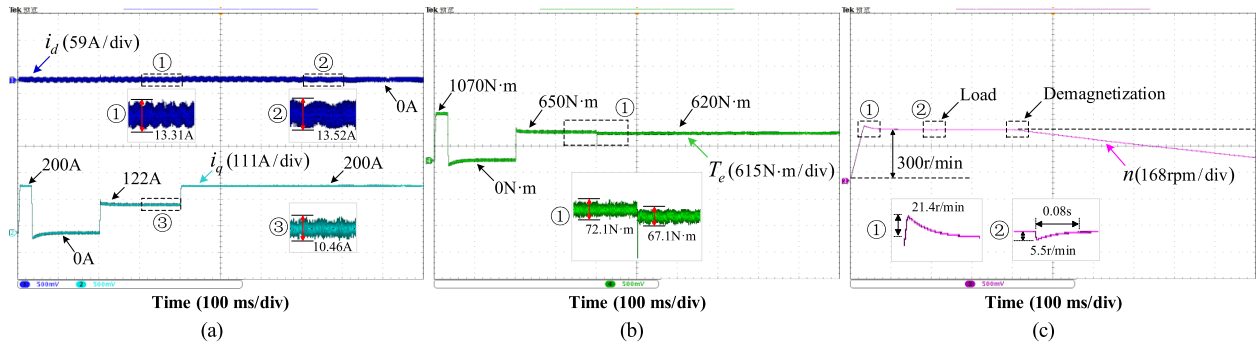

Fig. 10. Experimental results of SMC without DFTPC algorithm. (a) *dq*-axis current. (b) Electromagnetic torque. (c) Speed.

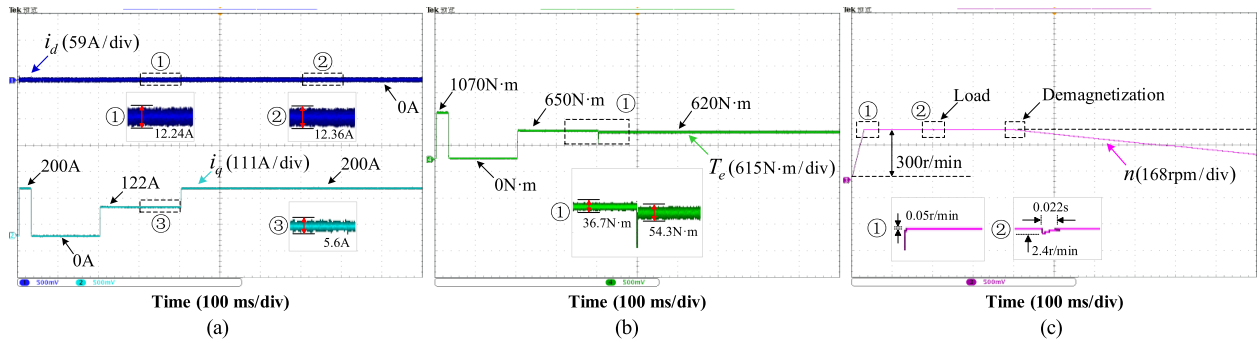

Fig. 11. Experimental results of the IEST-SMDO-based NFTSMC without DFTPC algorithm. (a) *dq*-axis current. (b) Electromagnetic torque. (c) Speed.

TABLE III
PARAMETERS OF OBSERVER

EST-SMDO	IEST-SMDO	SMO	NFTSMO	IST-NFTSMO
$k_a = 5000$	$k_a = 5000$	$k_d = 50000$	$\alpha = 200$	$\alpha = 200$
$k_b = 5000$	$k_b = 5000$	$k_q = 50000$	$\beta = 200$	$\beta = 200$
$k_c = 5000$	$k_c = 5000$	-	$\lambda = 4$	$\lambda = 4$
$G = 250$	$k_d = 10$	-	$\mu = 0.01$	$\mu = 0.01$
-	$G = 250$	-	$m/r = 5/3$	$m/r = 5/3$
-	-	-	$p/q = 7/5$	$p/q = 7/5$
-	-	-	$k_1 = 6500$	$k_1 = 0.1$
-	-	-	$k_2 = 5$	$k_2 = 6500$
-	-	-	-	$k_3 = 0.1$
-	-	-	-	$k_4 = 0.1$

electromagnetic torque curves, and Figs. 9(c), 10(c), and 11(c) show the speed curves, respectively.

From Figs. 9–11, the IEST-SMDO-based NFTSMC method reaches the steady state speed at 0.04 s, while the PI and SMC methods reach steady state 300 r/min at 0.1 s and 0.14 s, respectively. The speed overshoot of the SMC and the PI methods at no-load start-up is 7.13% and 0.14%, respectively, while the IEST-SMDO-based NFTSMC method's speed has almost no overshoot, and the corresponding i_q quickly recovers to the steady-state value after reaching the rated value in a short period of time, respectively. At 0.2 s, T_L is loaded from 0 to 650 N.m, the speed of PI, SMC and the IEST-SMDO-based NFTSMC drop by 7 r/min, 5.5 r/min and 2.4 r/min, respectively, and finally recover to the steady state value at 0.32 s, 0.28 s, and 0.22 s, respectively. As can be seen the speed of the proposed

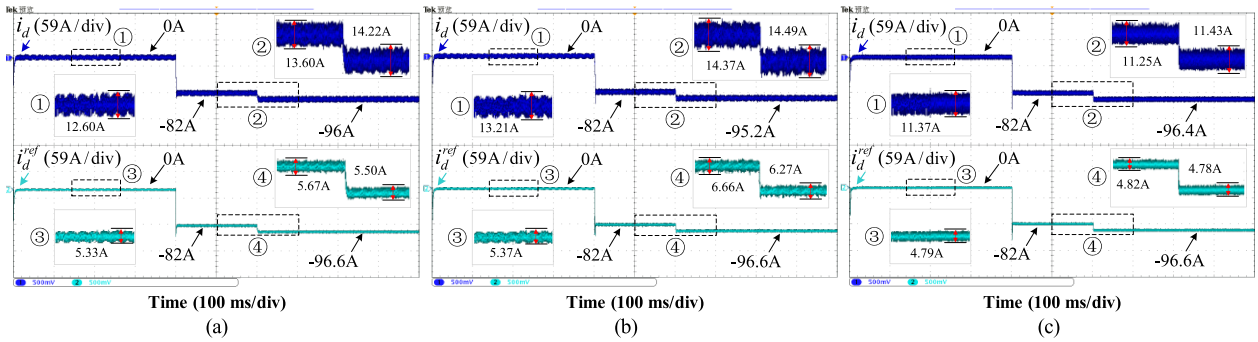

Fig. 12. Experimental results of the d-axis currents and the d-axis reference currents. (a) DFTPC-PI. (b) DFTPC-SMC. (c) DFTPC-IEST-SMDO-NFTSMC.

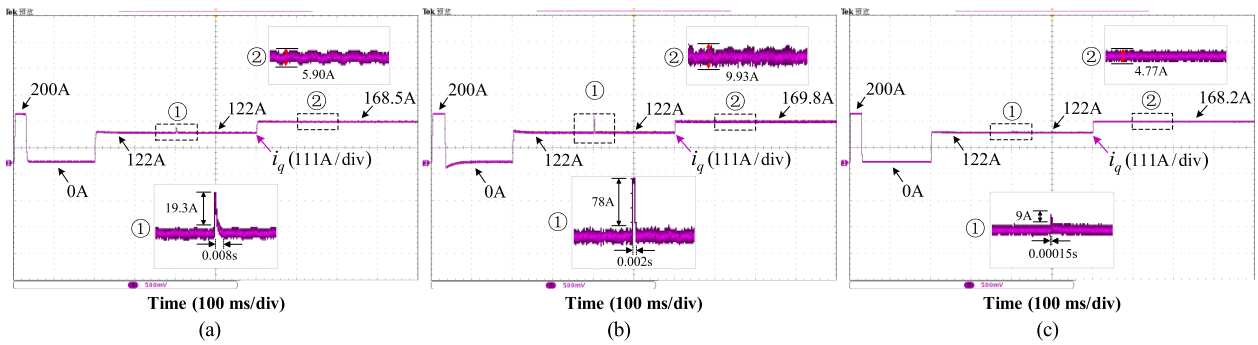

Fig. 13. Experimental results of the dq-axis currents. (a) DFTPC-PI. (b) DFTPC-SMC. (c) DFTPC-IEST-SMDO-NFTSMC.

IEST-SMDO-based NFTSMC method shows less fluctuation and faster recovery when T_L increases. The corresponding i_q reach the steady-state value of 122 A at 0.28 s, 0.24 s, and 0.22 s, and its T_e reaches the steady-state value of 650 N.m at 0.28 s, 0.24 s and 0.22 s, respectively. The results show compared with the remaining two methods, the IEST-SMDO-based NFTSMC method has better dynamic response.

At 0.4 s, the PM is demagnetized, and the i_q of the PI, SMC, and the IEST-SMDO-based NFTSMC increase rapidly to the limit value of 200 A, which is insufficient to maintain the stability of T_e. At this moment, the output T_e of the three methods are only 620 N.m, which is smaller than T_L. This leads to a sharp drop in speed that cannot track a given speed.

In summary, during normal motor operation, the proposed IEST-SMDO-based NFTSMC method has smaller overshoot and faster dynamic response than the conventional PI and SMC methods. However, due to the lack of adjustment by the DFTPC algorithm, the IEST-SMDO-based NFTSMC method still fails to make the motor operate normally when demagnetization fault occurs in the IPMSM.

B. IPMSM Control With DFTPC Algorithm

In order to compare the three methods (DFTPC-PI, DFTPC-SMC, and the proposed DFTPC-IEST-SMDO-NFTSMC) in the case of using the proposed DFTPC algorithm and to verify the fault tolerant capability of the proposed DFTPC algorithm (whether it is able to drive a heavy load when the PM is demagnetized), the operating conditions are set as follows.

The total experimental time is 1 s, the motor starts with no load and the reference speed N_r^{ref} is 300 r/min. The load torque T_L is loaded from 0 to 650 N.m (65% rated load) at 0.2 s. At 0.4 s, the IPMSM is demagnetized, and the flux linkage amplitude of PM ψ_{ro} decreases from 0.892 to 0.6 Wb (demagnetization 33%), while the magnetic deviation angle γ is changed from 0 to $\pi/6$ rad. At 0.6 s, T_L is loaded from 650 to 900 N.m (90% rated load).

Figs. 12, 13, 14, and 15 show the experimental results of PI control, SMC, and the IEST-SMDO-based NFTSMC with DFTPC algorithm during IPMSM demagnetization fault, respectively. Among them, Fig. 12(a), (b), and (c), respectively, shows the comparison curves of d-axis current and d-axis reference current for DFTPC-PI, DFTPC-SMC, and DFTPC-IEST-SMDO-NFSMC methods. Fig. 13(a), (b), and (c), respectively, shows the q-axis current response curves of the three methods. Fig. 14(a), (b), and (c) and Fig. 15(a), (b), and (c), respectively, display the output speed and torque curves of the three methods.

Before 0.4 s, the IPMSM is in normal operation and the output $i_d^{ref}(k+1)=0$. From Figs. 12–15, the experimental results of dq-axis current, torque and speed are the same as those in Figs. 9, 10, and 11.

At 0.4 s, the PM is demagnetized. From Fig. 12, the output value of $i_d^{ref}(k+1)$ under the three control modes decreases from 0 A to -82 A, with a theoretically calculated value -82.1 A, indicating that the DFTPC algorithm is able to accurately calculate$i_d^{ref}(k+1)$. When T_L is 650 N.m, the calculated constraint value of i_d is -158.4 A, indicating that $i_d^{ref}(k+1)$ is within the constraint range.

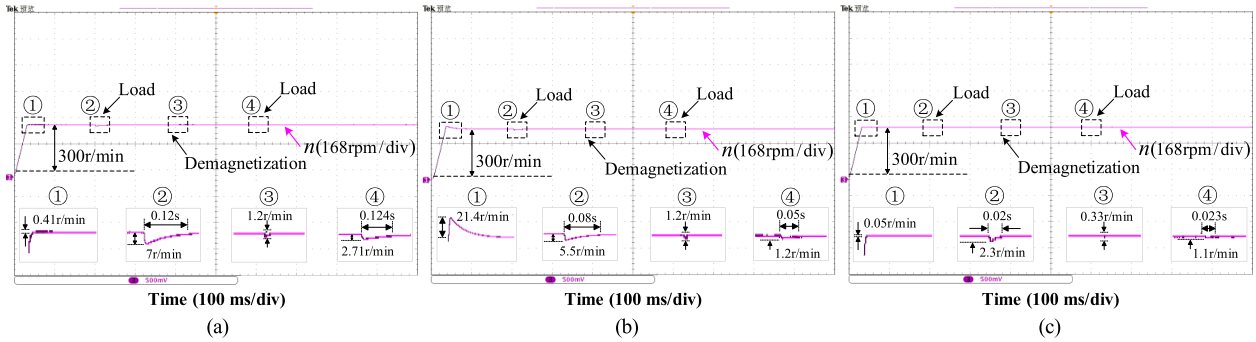

Fig. 14. Experimental results of the speed. (a) DFTPC-PI. (b) DFTPC-SMC. (c) DFTPC-IEST-SMDO-NFTSMC.

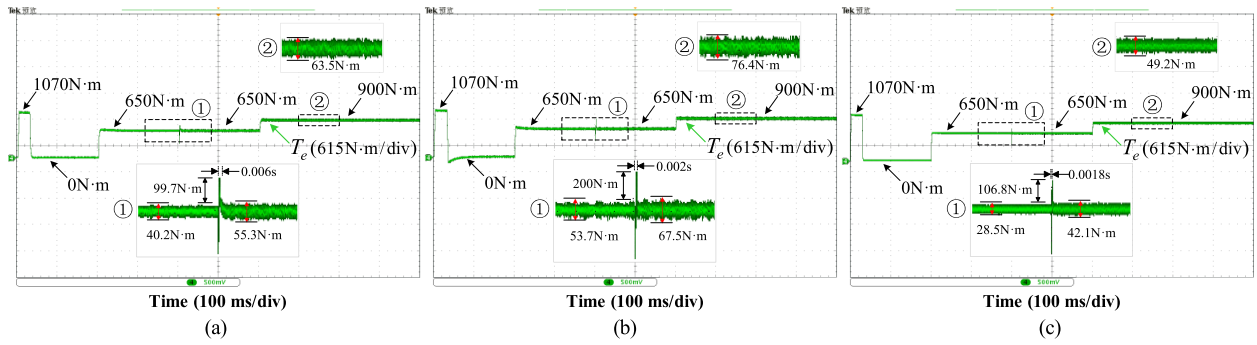

Fig. 15. Experimental results of the output torque. (a) DFTPC-PI. (b) DFTPC-SMC. (c) DFTPC-IEST-SMDO-NFTSMC.

From Fig. 13, the i_q of the three methods rises by 19 A, 78 A, and 9 A at 0.4 s, and finally returns to the steady state value of 122 A during normal operation at 0.408 s, 0402 s, and 0.4015 s, respectively. This indicates after using the DFTPC algorithm, the i_q of the motor in case of demagnetization fault does not rise abruptly, and quickly recovers to normal values. The current loss of control is effectively suppressed. The i_q in the proposed DFTPC-IEST-SMDO-NFTSMC method is recovered faster and with less fluctuation than the other two methods. From Fig. 14, the speeds of the three methods drop by 1.2 r/min, 1.2 r/min, and 0.33 r/min at 0.4 s, and finally return to steady state at 0.405 s, 0.406 s, and 0.402 s, respectively. From Fig. 15, the T_e of all three methods can recover to 650 N.m quickly. However, compared to the other two methods, the T_e of the proposed DFTPC-IEST-SMDO-NFTSMC method exhibits faster recovery and smaller fluctuations at the moment of PM demagnetization. The results indicate the DFTPC-IEST-SMDO-NFTSMC method has better dynamic response under motor demagnetization fault. Its ripple of current and torque is smaller, and the waveforms are smoother.

At 0.6 s, T_L is loaded from 650 to 900 N.m. From Fig. 12, the output value of $i_d^{ref}(k+1)$ decreases from -82 A to -96.6 A with a theoretical value of -96.4 A, while the constrained value of i_d is calculated to be -108.2 A when T_L is 900 N.m. The results show $i_d^{ref}(k+1)$ is still within the constraint range. From Fig. 13, the i_q of the three methods reaches steady-state values of 168.5 A, 169.8 A and 168.2 A at 0.61 s, 0.606 s, and 0.603 s, respectively. From Fig. 14, the speeds of the three methods decrease by 2.71 r/min, 1.2 r/min, and 1.1 r/min, and finally recover to the steady state values at 0.724 s, 0.65 s, and 0.623 s,

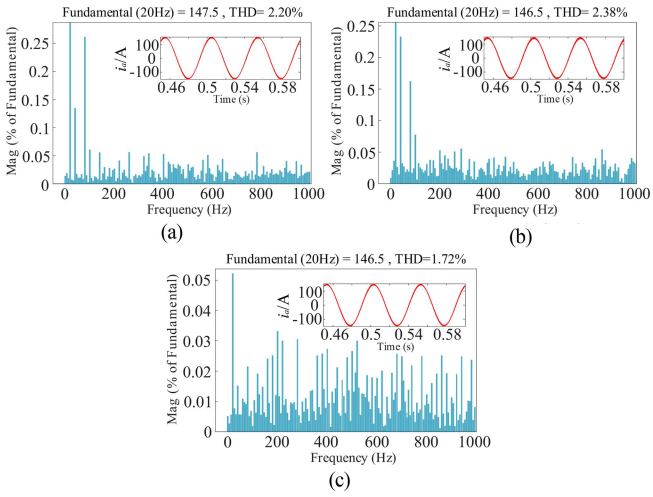

Fig. 16. THD analysis of A phase stator current. (a) DFTPC-PI control. (b) DFTPC-SMC. (c) DFTPC-IEST-SMDO-NFTSMC.

respectively. From Fig. 15, the T_e of the three methods reaches steady-state values of 900 N.m at 0.61 s, 0.606 s, and 0.603 s, respectively. The results show that when the PM is demagnetized, the DFTPC algorithm enables the motor to drive the 90% rated load to operate normally with strong fault tolerant capability. The proposed DFTPC-IEST-SMDO-NFTSMC method shows lower current and torque ripple and faster dynamic response under the large load operating condition.

TABLE IV
PERFORMANCE COMPARISON OF VARIOUS CONTROL METHODS OVER THE ENTIRE LOAD RANGE

Load	THD/(%)	Torque ripple/(%)	Load	THD/(%)	Torque ripple/(%)
5% rated load	19.78/23.01/16.82	33.13/40.68/28.77	55% rated load	2.57/2.74/2.00	4.37/6.03/3.65
10% rated load	12.37/16.43/10.83	17.08/28.72/13.37	60% rated load	2.36/2.58/1.81	4.20/5.73/3.47
15% rated load	8.38/11.76/6.84	12.57/21.83/10.58	65% rated load	2.20/2.38/1.72	4.12/5.25/3.33
20% rated load	7.13/8.03/4.90	9.92/15.87/7.94	70% rated load	2.05/2.23/1.56	3.88/5.10/3.12
25% rated load	5.45/6.10/3.98	8.93/12.42/6.75	75% rated load	1.95/2.09/1.51	3.90/4.80/2.98
30% rated load	4.44/5.02/3.38	7.10/10.71/5.46	80% rated load	1.84/1.99/1.44	3.67/4.65/2.85
35% rated load	3.79/4.26/2.91	6.33/8.84/4.99	85% rated load	1.78/1.90/1.35	3.48/4.63/2.68
40% rated load	3.34/3.72/2.61	5.58/7.95/4.53	90% rated load	1.70/1.82/1.31	3.41/4.27/2.74
45% rated load	3.02/3.33/2.34	4.96/7.10/4.13	95% rated load	-	-
50% rated load	2.76/2.99/2.14	4.67/6.62/3.87	100% rated load	-	-

Remark 4: *The data in the table are derived under IPMSM demagnetization condition (demagnetization 33%, γ change $\pi/6$ rad), where 1/2/3 are the following three methods: DFTPC-PI, DFTPC-SMC, and DFTPC-IEST-SMDO-NFTSMC.*

Fig. 16(a), (b), and (c) shows the total harmonic distortion (THD) analysis of the A-phase stator current for the three methods under the condition of PM demagnetization and T_L of 650 N.m, respectively. The waveform analysis shows the THD of the three methods are 2.20%, 2.38%, and 1.72%, respectively. The results show the proposed DFTPC-IEST-SMDO-NFTSMC method can effectively suppress the current harmonics of the IPMSM after a demagnetization fault occurs, relative to the DFTPC-PI and DFTPC-SMC methods.

The performance comparison of all control methods over the entire load range is shown in Table IV. In Table IV, because the proposed DFTPC method achieves fault-tolerant control by adjusting the i_d rather than magnetising the PM material. Therefore, when the T_L increases above 95% of the rated load and the PM is demagnetized (demagnetization 33%, γ change $\pi/6$ rad), due to the limited output capability of the inverter, DFTPC-PI, DFTPC-SMC, and DFTPC-IEST-SMDO-NFTSMC methods are unable to compensate for the torque deficit caused by the demagnetization.

In summary, the DFTPC algorithm exhibits stronger fault tolerance in the control system and is able to drive larger loads in case of IPMSM demagnetization fault. Compared with the DFTPC-PI and DFTPC-SMC methods, the DFTPC-IEST-SMDO-NFTSMC method shows less speed fluctuation, faster response, more stable torque and *dq*-axis current waveforms, fewer harmonics, and stronger anti-interference capability.

The theoretical comparison of all methods is shown in Table V.

TABLE V
THEORETICAL COMPARISON OF METHODS

Indicators	Methods	Values
Convergence time	DFTPC-PI	N: 0.1s/0.32s/0.405s/0.124s
		i_q: 0.04s/0.08s/0.008s/0.1s
		T_e: 0.038s/0.08s/0.006s/0.046s
	DFTPC-SMC	N: 0.14s/0.28s/0.406s/0.05s
		i_q:0.09s/0.05s/0.002s/0.04s
		T_e: 0.1s/0.06s/0.0025s/0.05s
	DFTPC-IEST-SMDO-NFTSMC	N: 0.04s/0.22s/0.402s/0.023s
		i_q:0.034s/0.02s/0.00015s/0.03s
		T_e: 0.034s/0.02s/0.002s/0.03s
Overshoot and undershoot	DFTPC-PI	N/(r/min): 0.41/7/1.2/2.71
		i_q/(A): 0.42/4.13/19.3/0.91
		T_e/(N·m): 2/15.34/99.73/9.1
	DFTPC-SMC	N/(r/min): 21.4/5.5/1.2/1.2
		i_q/(A): 18.78/7.04/78/0.26
		T_e/(N·m): 27.22/34.7/200/10.5
	DFTPC-IEST-SMDO-NFTSMC	N/(r/min): 0.05/2.3/0.33/1.1
		i_q/(A): 0.09/2.27/9.03/0.2
		T_e/(N·m): 0.84/10.73/106.8/5.4
Number of parameters	DFTPC-PI	12
	DFTPC-SMC	12
	DFTPC-IEST-SMDO-NFTSMC	20

Remark 5: *1/2/3/4 are the values corresponding to the variables of the motor in the following four states: 1) no-load start, 2) loading to 650N·m, 3) Demagnetization (demagnetization 33%, γ change $\pi/6$ rad), 4) loading to 900N·m.*

C. Experimental Results of the Flux Linkage Observer

The comparison experimental waveforms of SMO, NFTSMO, and IST-NFTSMO are shown in Fig. 17. Among them, Fig. 17(a) and (b) shows the *dq*-axis flux linkages waveforms observed by SMO, NFTSMO, and IST-NFTSMO, respectively.

The motor is started with no load before 0.4 s. From Fig. 17(a), the ψ_{rd} observation of SMO reaches the steady state value of 0.8917 Wb at 0.09 s, while the ψ_{rd} observation of NFTSMO and IST-NFTSMO reaches the steady state value of 0.892 Wb at 0.11 s and 0.08 s, respectively. From Fig. 17(b), the ψ_{rq} observation of the three observers can maintain 0 Wb, and the theoretically calculated values of ψ_{rd} and ψ_{rq} are 0.892 Wb and 0 Wb, respectively, showing that the designed observer can accurately observe the flux linkage of the motor during normal operation, and the observation speed is faster.

At 0.2 s, T_L is loaded from 0 to 650 N.m, and the ψ_{rd} observed by SMO, NFTSMO, and IST-NFTSMO rises by 0.00285 Wb, 0.0016 Wb, and 0.0006 Wb, respectively, and eventually at 0.224 s, 0.22 s, and 0.215 s, respectively, return to steady state, while the ψ_{rq} observed by the three observers remains almost

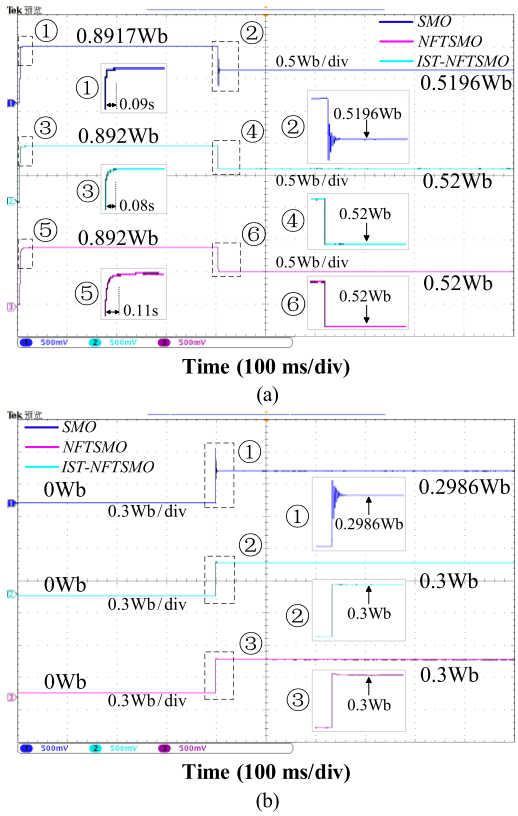

Fig. 17. Experimental results of the flux linkage observer. (a) Comparison of d-axis flux linkage. (b) Comparison of q-axis flux linkage.

TABLE VI
COMPARISON OF THE PERFORMANCE OF FLUX LINKAGE OBSERVERS-D-AXIS

Performance indicators	Observers	Values
Flux linkage convergence time (s)	SMO	0.09/0.224/0.46/0.632
	NFTSMO	0.11/0.22/0.46/0.602
	IST-NFTSMO	0.08/0.215/0.44/0.601
Flux linkage steady state value (Wb)	SMO	0.8917/0.8917/0.5207/0.5207
	NFTSMO	0.892/0.892/0.52/0.52
	IST-NFTSMO	0.892/0.892/0.52/0.52

Remark 6: *1/2/3/4 are the values corresponding to the variables of the motor in the following four states: 1) no-load operation, 2) loading to 650N·m, 3) Demagnetization (demagnetization 33%, γ change π/6 rad), 4) loading to 900N·m.*

TABLE VII
COMPARISON OF THE PERFORMANCE OF FLUX LINKAGE OBSERVERS-Q-AXIS

Performance indicators	Observers	Values
Flux linkage convergence time (s)	SMO	0/0.2/0.48/0.635
	NFTSMO	0/0.2/0.49/0.603
	IST-NFTSMO	0/0.2/0.48/0.602
Flux linkage steady state value (Wb)	SMO	0/0/0.2986/0.2986
	NFTSMO	0/0/0.3/0.3
	IST-NFTSMO	0/0/0.3/0.3

Remark 7: *1/2/3/4 are the values corresponding to the variables of the motor in the following four states: 1) no-load operation, 2) loading to 650N·m, 3) Demagnetization (demagnetization 33%, γ change π/6 rad), 4) loading to 900N·m.*

unchanged. The results show the designed observer has a faster convergence rate.

At 0.4 s, the PM is demagnetized. The ψ_{rd} observation of SMO reaches the steady state value of 0.5207 Wb at 0.46 s, while the ψ_{rd} observations of NFTSMO and IST-NFTSMO reach the steady state value of 0.52 Wb at 0.46 s and 0.44 s, respectively. The ψ_{rq} observation of SMO reaches the steady state value of 0.2986 Wb at 0.48 s, while the ψ_{rq} observations of NFTSMO and IST-NFTSMO reach the steady state value of 0.3 Wb at 0.49 s and 0.48 s, respectively. In addition, at the moment of demagnetization of the PM, SMO produces a large jitter and NFTSMO shows a certain degree of overshooting. Compared with the two, the observed waveforms of the designed IST-NFTSMO are much more stable and almost free of overshooting. The theoretical calculated values of ψ_{rd} and ψ_{rq} are $0.6\cos(\pi/6) = 0.5196$ Wb and $0.6\sin(\pi/6) = 0.3$ Wb, respectively, it is shown that the designed observer achieves accurate observation of motor fault flux linkage.

At 0.6 s, the T_L is loaded from 650 to 900 N.m, and the ψ_{rd} observed by SMO, NFTSMO, and IST-NFTSMO rises by 0.0015 Wb, 0.0004 Wb, and 0.00015 Wb, respectively, and finally at 0.632 s, 0.602 s, and 0.601 s, respectively, returns to steady state, while the ψ_{rq} observed by the three observers remains almost at the steady state value.

In summary, the observation of the flux linkage by the designed IST-NFTSMO is faster, the flux linkage waveform is smoother, and the chattering is reduced. In comparison with SMO and NFTSMO, IST-NFTSMO demonstrates a better dynamic performance, less chattering, and higher robustness.

Tables VI and VII show the performance comparison of the flux linkage observer for the d- and q-axis flux linkage observation, respectively.

D. Experimental Results of the Disturbance Observer

Fig. 18 shows the observed waveforms of EST-SMDO and IEST-SMDO for the total system disturbance, where Fig. 18(a) shows the observed waveforms of IEST-SMDO and EST-SMDO, and Fig. 18(b) shows the comparative waveforms of EST-SMDO and IEST-SMDO for the disturbance observation, respectively.

From Fig. 18, the IPMSM is run unloaded until 0.2 s, the IEST-SMDO shows much smaller overshoots. At 0.2 s, T_L is loaded from 0 to 650 N.m. It can be clearly seen the designed IEST-SMDO observes the disturbance faster. At this moment, the theoretical value of the disturbance is basically equal to T_L. The results show the designed IEST-SMDO can more accurately observe the disturbances of the motor during normal operation.

At 0.4 s, the PM is demagnetized. The disturbance observation values of EST-SMDO and IEST-SMDO both recovered to steady-state values of 652 and 651.5 after a small fluctuation, respectively. At this time, the theoretical calculated value is 650.324. It shows the designed IEST-SMDO can accurately

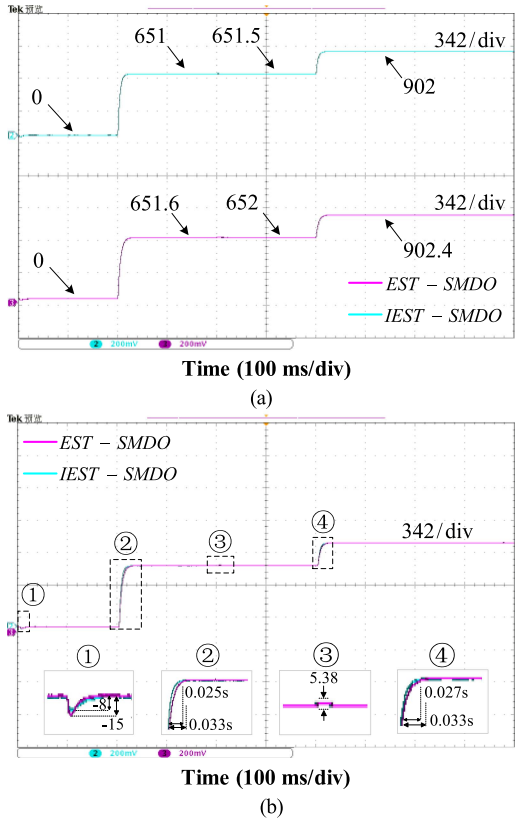

Fig. 18. Experimental results of the disturbance observer. (a) IEST-SMDO and EST-SMDO. (b) Comparison between IEST-SMDO and EST-SMDO.

TABLE VIII
PERFORMANCE COMPARISON OF DISTURBANCE OBSERVERS

Performance indicators	Observers	Values
Disturbance convergence time (s)	EST-SMDO	0.045/0.233/0.416/0.633
	IEST-SMDO	0.041/0.225/0.15/0.627
Disturbance steady state value (Wb)	EST-SMDO	0/651.6/652/902.4
	IEST-SMDO	0/651/651.5/902

Remark 8: *1/2/3/4 are the values corresponding to the variables of the motor in the following four states: 1) no-load operation, 2) loading to 650N·m, 3) Demagnetization (demagnetization 33%, γ change π/6 rad), 4) loading to 900N·m.*

observe the disturbances of the motor during demagnetization fault.

In summary, compared with EST-SMDO, the designed IEST-SMDO can observe the system total disturbance caused by load changes, PM demagnetization and the action of the DFTPC algorithm more accurately with better dynamic response, and the anti-interference ability of the system is effectively boosted.

Table VIII shows the performance comparison of the disturbance observer.

VII. CONCLUSION

Aiming at the issues of torque degradation, poor robustness, and slow response of IPMSM after the occurrence of demagnetization fault, an IST-NFTSMO-based DFTPC strategy for IPMSM demagnetization fault is proposed. The proposed method can compensate for the torque loss caused by demagnetization fault, enable the system's fault-tolerance, robustness, and response speed to be enhanced. Through the experimental analysis of different working conditions, the following conclusions are drawn.

1) The designed IST-NFTSMO can observe the *dq*-axis flux linkages of IPMSM more quickly and accurately. After demagnetization of the PM, the observation of flux linkage can quickly converge, and the chattering caused by conventional NFTSMO is suppressed. The observed flux linkage is fed into the controller, and thus the effects of flux linkage parameter mismatch to be eliminated.
2) The proposed DFTPC algorithm combined with conventional PI and SMC methods can timely output the *d*-axis reference current for the next moment after motor demagnetization, thereby the missing torque is compensated and the sudden rise of i_q is suppressed. This ensures the normal operation of the motor under demagnetization fault, and can drive a larger load with stronger fault-tolerance capability.
3) The IEST-SMDO is designed to observe motor disturbances more quickly and accurately and perform feedforward compensation, the immunity of the system is boosted. DFTPC-IEST-SMDO-NFTSMC has faster response and better steady state performance. When the demagnetization fault occurs, the THD under whole load range of DFTPC-IEST-SMDO-NFTSMC is reduced by an average of 20% and 32.2%, and the torque ripple is suppressed by an average of 18.5% and 42.8% when compared with DFTPC-PI and DFTPC-SMC, further enhancing the robustness of the system.

In addition, since the proposed method adjusts the parameters by empirical method, further optimization of the design of the parameters will be the next research work.

REFERENCES

[1] Q. Hou, Y. Zuo, J. Sun, C. H. Lee, Y. Wang, and S. Ding, "Modified nonlinear active disturbance rejection control for PMSM speed regulation with frequency domain analysis," *IEEE Trans. Power Electron.*, vol. 38, no. 7, pp. 8126–8134, Jul. 2023.
[2] F. Wang, Y. Wei, H. Young, D. Ke, H. Xie, and J. Rodriguez, "Continuous-control-set model-free predictive fundamental current control for PMSM system," *IEEE Trans. Power Electron.*, vol. 38, no. 5, pp. 5928–5938, May 2023.
[3] P. Luo, Z. Yin, Z. Zhang, Y. Zhang, P. Zhang, and J. Liu, "Diversified diagnosis strategy for PMSM inter-turn short-circuit fault via novel sliding mode observer," *IEEE Trans. Power Electron.*, vol. 39, no. 4, pp. 4149–4159, Apr. 2024.
[4] Y. Wei, H. Young, D. Ke, D. Huang, F. Wang, and J. Rodríguez, "Adaptive ultra-localized time-series for improved model-free predictive current control on PMSM drives," *IEEE Trans. Power Electron.*, vol. 39, no. 5, pp. 5155–5165, May 2024.
[5] Y. Han, S. Chen, C. Gong, X. Zhao, F. Zhang, and Y. Li, "Accurate SM disturbance observer-based demagnetization fault diagnosis with parameter mismatch impacts eliminated for IPM motors," *IEEE Trans. Power Electron.*, vol. 38, no. 5, pp. 5706–5710, May 2023.
[6] M. Baranski, W. Szelag, and W. Lyskawinski, "Experimental and simulation studies of partial demagnetization process of permanent magnets in electric motors," *IEEE Trans. Energy Convers.*, vol. 36, no. 4, pp. 3137–3145, Dec. 2021.

[7] S. S. Moosavi et al., "Demagnetization fault diagnosis in permanent magnet synchronous motors: A review of the state-of-the-art," *J. Magnetism Magn. Mater.*, vol. 391, pp. 203–212, Jan. 2015.

[8] D. Li et al., "Irreversible demagnetization of a large capacity line-start permanent magnet synchronous motors considering influence of permanent magnet temperature," *Int. Trans. Elect. Energy Syst.*, vol. 2023, Aug. 2023, Art. no. 6798493.

[9] X. Xiao, C. Chen, and M. Zhang, "Dynamic permanent magnet flux estimation of permanent magnet synchronous machines," *IEEE Trans. Appl. Supercond.*, vol. 20, no. 3, pp. 1085–1088, Jun. 2010.

[10] Y. W. Youn, D. H. Hwang, S. J. Song, and Y. H. Kim, "Detection and classification of demagnetization and short-circuited turns in permanent magnet synchronous motors," *J. Elect. Eng. Technol.*, vol. 13, no. 4, pp. 1614–1622, Jul. 2018.

[11] X. Song, J. Zhao, J. Song, F. Dong, L. Xu, and J. Zhao, "Local demagnetization fault recognition of permanent magnet synchronous linear motor based on S-transform and PSO–LSSVM," *IEEE Trans. Power Electron.*, vol. 35, no. 8, pp. 7816–7825, Aug. 2020.

[12] Z. Chen, K. Gryllias, and W. Li, "Mechanical fault diagnosis using convolutional neural networks and extreme learning machine," *Mech. Syst. Signal Process.*, vol. 133, no. 1, Nov. 2019, Art. no. 106272.

[13] J. Cen, Z. Chen, Y. Wu, and Z. Yang, "Intelligent machine fault diagnosis based on deep transfer convolutional neural network and extreme learning machine," *Proc. Inst. Mech. Engineers, C, J. Mech. Eng. Sci.*, vol. 237, no. 9, pp. 2201–2212, Nov. 2023.

[14] Z. Liu, Q. Xia, L. Chen, H. Zhang, C. Wang, and X. Li, "Demagnetization fault diagnosis of PMSM based on fuzzy extreme learning machine," in *Proc. Chin. Automat. Congr.*, 2020, pp. 5690–5695.

[15] J. Song et al., "Demagnetization modeling research for permanent magnet in PMSLM using extreme learning machine," in *Proc. IEEE Int. Electric Machines Drives Conf.*, 2019, pp. 1757–1761.

[16] J. A. Rosero, J. Cusido, A. Garcia, J. A. Ortega, and L. Romeral, "Study on the permanent magnet demagnetization fault in permanent magnet synchronous machines," in *Proc. IEEE 32nd Annu. Conf. Ind. Electron.*, 2019, pp. 879–884.

[17] P. Pietrzak and M. Wolkiewicz, "Demagnetization fault diagnosis of permanent magnet synchronous motors based on stator current signal processing and machine learning algorithms," *Sensors*, vol. 23, no. 4, Feb. 2023, Art. no. 1757.

[18] X. Xiao, C. Chen, and M. Zhang, "Dynamic permanent magnet flux estimation of permanent magnet synchronous machines," *IEEE Trans. Appl. Supercond.*, vol. 20, no. 3, pp. 1085–1088, Jun. 2010.

[19] T. Wang, B. Wang, Y. Yu, and D. Xu, "Discrete sliding-mode-based MRAS for speed-sensorless induction motor drives in the high-speed range," *IEEE Trans. Power Electron.*, vol. 38, no. 5, pp. 5777–5790, May 2023.

[20] X. Yan and M. Cheng, "An MRAS observer-based speed sensorless control method for dual-cage rotor brushless doubly fed induction generator," *IEEE Trans. Power Electron.*, vol. 37, no. 10, pp. 12705–12714, Oct. 2022.

[21] S. Huang, G. Wu, F. Rong, C. Zhang, S. Huang, and Q. Wu, "Novel predictive stator flux control techniques for PMSM drives," *IEEE Trans. Power Electron.*, vol. 34, no. 9, pp. 8916–8929, Sep. 2019.

[22] J. Zhao, L. Wang, L. Xu, F. Dong, J. Song, and X. Yang, "Uniform demagnetization diagnosis for permanent-magnet synchronous linear motor using a sliding-mode velocity controller and an ALN-MRAS flux observer," *IEEE Trans. Ind. Electron.*, vol. 69, no. 1, pp. 890–899, Jan. 2022.

[23] K. H. Zhao, T. F. Chen, C. F. Zhang, J. He, and G. Huang, "Online fault detection of permanent magnet demagnetization for ipmsms by nonsingular fast terminal-sliding-mode observer," *Sensors*, vol. 14, no. 12, pp. 23119–23136, Dec. 2014.

[24] Y. Zafari, A. H. Mazinan, and S. Shoja-Majidabad, "Demagnetization fault detection for five-phase IPMSM through integral terminal sliding mode flux-linkage observer," *IETE J. Res.*, vol. 64, no. 4, pp. 473–486, Sep. 2019.

[25] J. Gao, W. Gui, C. Yang, T. Peng, J. Luo, and Y. Han, "Multiple observers-based demagnetization fault detection with inductance mismatch impacts eliminated for PMSMs," *IEEE Trans. Power Electron.*, vol. 38, no. 7, pp. 8016–8021, Jul. 2023.

[26] K. Zhao, W. Dai, S. Wu, P. Qiu, W. Liu, and G. Huang, "Improved super-twisting-observer-based finite-control-set model-predictive fault-tolerant current control of PMSM considering demagnetization fault," *Int. J. Elect. Power Energy Syst.*, vol. 142, Nov. 2022, Art. no. 108325.

[27] C. Zhang, G. Wu, J. He, J. Feng, and K. Zhao, "Fault-tolerant predictive control for demagnetization faults in permanent magnet synchronous machine," *Trans. China Electrotechnical Soc.*, vol. 32, no. 15, pp. 100–110, Aug. 2017.

[28] K. Zhao, R. Zhou, A. Leng, K. Dai, and G. Hang, "Finite control set model-free fault-tolerant predictive control for permanent magnet synchronous motor," *Trans. China Electrotechnical Soc.*, vol. 36, no. 1, pp. 27–38, Jan. 2021.

[29] F. Hu, D. Luo, C. Luo, Z. Long, and G. Wu, "Cascaded robust fault-tolerant predictive control for PMSM drives," *Energies*, vol. 11, no. 11, Nov. 2018, Art. no. 3087.

[30] K. Zhao et al., "Demagnetization-fault reconstruction and tolerant-control for PMSM using improved SMO-based equivalent-input-disturbance approach," *IEEE/ASME Trans. Mechatron.*, vol. 27, no. 2, pp. 701–712, Apr. 2022.

[31] G. Huang, J. Li, E. F. Fukushima, C. Zhang, J. He, and K. Zhao, "An improved equivalent-input-disturbance approach for PMSM drive with demagnetization fault," *Instrum. Soc. Amer. Trans.*, vol. 105, no. 2020, pp. 120–128, Oct. 2020.

[32] C. Zhang, G. Wu, J. He, and K. Zhao, "Sliding observer-based demagnetisation fault-tolerant control in permanent magnet synchronous motors," *J. Eng. Mech.*, vol. 6, no. 2017, pp. 175–183, Apr. 2017.

[33] J. Lei, S. Fang, D. Huang, and Y. Wang, "Enhanced deadbeat predictive current control for PMSM drives using iterative sliding mode observer," *IEEE Trans. Power Electron.*, vol. 38, no. 11, pp. 13866–13876, Nov. 2023.

[34] I. Boldea, M. C. Paicu, and G.-D. Andreescu, "Active flux concept for motion-sensorless unified AC drives," *IEEE Trans. Power Electron.*, vol. 23, no. 5, pp. 2612–2618, Sep. 2008.

[35] K. Zhao, A. Leng, R. Zhou, W. Dai, S. Wu, and T. Li, "Demagnetization fault reconstruction for six-phase permanent magnet synchronous motor by improved super-twisting algorithm-based sliding-mode observer," *Measurement*, vol. 172, Feb. 2021, Art. no. 108905.

[36] Y. Yang and S. Qin, "A new modified super-twisting algorithm with double closed-loop feedback regulation," *Trans. Inst. Meas. Control*, vol. 39, no. 11, pp. 1603–1612, Apr. 2016.